Key Points:
- Coupled forward geomechanical modeling of thrust and fold evolution including syntectonic sedimentation is developed
- Significance of overpressure in structural deformation style is shown
- Overpressure and porosity predicted by geomechanical models are more accurate than those estimated by 1-D methods

Correspondence to:
M. Rouainia,
m.rouainia@ncl.ac.uk

Hydromechanical Modeling of Stress, Pore Pressure, and Porosity Evolution in Fold-and-Thrust Belt Systems

J. Obradors-Prats[1], M. Rouainia[1] [iD], A. C. Aplin[2], and A. J. L. Crook[3]

[1]School Engineering, Newcastle University, Newcastle upon Tyne, UK, [2]Department of Earth Sciences, Durham University, Durham, UK, [3]Three Cliffs Geomechanical Analysis, Swansea, UK

Abstract We present coupled, critical state, geomechanical-fluid flow simulations of the evolution of a fold-and-thrust belt in NW Borneo. Our modeling is the first to include the effects of both syntectonic sedimentation and transient pore pressure on the development of a fold-and-thrust belt. The present-day structure predicted by the model contains the key first-order structural features observed in the field in terms of thrust fault and anticline architectures. Stress predictions in the sediments show two compressive zones aligned with the shortening direction located at the thrust front and back limb. Between the compressive zones, near to the axial plane of the anticline, the modeled stress field represents an extensional regime. The predicted overpressure distribution is strongly influenced by tectonic compaction, with the maximum values located in the two laterally compressive regions. We compared the results at three notional well locations with their corresponding uniaxial strain models: the 2-D thrust model predicted porosities which are as much as 7.5% lower at 2.5 km depth and overpressures which are up to 6.4 MPa higher at 3 km depth. These results show that one-dimensional methods are not sufficient to model the evolution of pore pressure and porosity in contractional settings. Finally, we performed a drained simulation during which pore pressures were kept hydrostatic. The predicted geological structures differ substantially from those of the coupled simulation, with no thrust faulting. These results demonstrate that pore pressure is a key control on structural development.

1. Introduction

Fold-and-thrust belts are areas of major and complex structural deformation, the nature of which is strongly influenced by the way in which both material properties and fluid pressure evolve through geological time in response to changes in the stress regime and — for material properties — temperature. Given their importance and complexity, the formation and evolution of fold-and-thrust belt systems has been widely investigated using a range of techniques including physical modeling (Bose et al., 2014; Cobbold & Castro, 1999; McClay et al., 2004; Zanella et al., 2014), kinematic modeling (Cardozo & Brandenburg, 2014; Shaw et al., 1999; Suppe & Medwededd, 1990), and numerical modeling (Albertz & Lingrey, 2012; Albertz & Sanz, 2012; Smart et al., 2012; Thornton & Crook, 2014). Previous, geologically focused geomechanical modeling approaches to structural evolution have been generally limited by the fact that they have assumed hydrostatic pore pressures (Albertz & Lingrey, 2012; Albertz & Sanz, 2012; Nikolinakou et al., 2014; Smart et al., 2012). However, the evolving pore pressure regime is likely to play an important role in structural evolution, as overpressure has a direct influence on effective stress, which in turn exerts a significant influence on evolving material properties.

Since many fold-and-thrust belts host prolific hydrocarbon reservoirs (Aydin & Engelder, 2014; Beaudoin et al., 2014; Corredor et al., 2005; Mitra, 1990; Morley, 2009), there is also a strong practical reason to be able to predict both the stress regime and pore pressure distribution prior to drilling (Couzens-Schultz & Azbel, 2014; Hennig et al., 2002).

The prediction of pore pressure in sedimentary basins is often addressed using one-dimensional methods (e.g., Daniel, 2001; Hennig et al., 2002; van Ruth et al., 2002; Zhang, 2013), assuming that mechanical compaction is solely driven by the vertical effective stress exerted by the overburden (Hubbert & Rubey, 1959; Terzaghi, 1923). Even in cases where pore pressure evolution is modeled using basin models which incorporate 2-D or 3-D fluid flow, porosity loss is generally considered as being a simple function of vertical effective

stress (e.g., Allwardt et al., 2009; Flemings & Lupa, 2004). In this way, porosity is a function of vertical effective stress, which then allows pore pressure to be estimated. In addition, even state-of-the-art basin modeling software is not capable of modeling structural development as a result of tectonic activity, instead using prescribed geometries at specified geological times (e.g., Neumaier et al., 2014). These approaches to pore pressure evolution are unlikely to be sufficient in basins dominated by active tectonics such as fold-and-thrust belts or basins associated with salt diapirs, due to the contribution of lateral deformation and lateral stresses on compaction and overpressure generation (e.g., Couzens-Schultz & Azbel, 2014; Obradors-Prats et al., 2016). Analysis of the evolution of stress, pore pressure, and geological structures in fold-and-thrust belts should therefore be addressed using 2-D/3-D coupled hydromechanical procedures.

In this paper, we present 2-D plane strain, coupled fluid-flow, and geomechanical simulations of the evolution of a fold-and-thrust structure that for the first time includes syntectonic sedimentation and overpressure development due to tectonic compaction. We model the sediment rheology using critical state-based constitutive models that enable the simulation of strain hardening and strain softening with fault localization. Published data from the NW Borneo thrust belt is used to constrain and illustrate the performance of the proposed model and to provide reasonable values for the amount of shortening, the shortening rate, and the syntectonic sedimentation rate.

The key objectives of this study are to (1) investigate the importance of accounting for structural evolution in controlling the magnitude and distribution of stresses, porosity, and overpressure during tectonic deformation, and in turn (2) assess the influence of overpressure on structural development. To this end, we first analyze results obtained from a 2-D plane strain model and compare them with the solution obtained from 1-D methods. We then perform a drained simulation, in which pore pressures remain hydrostatic during the entire simulation and compare the structural development with that obtained from the coupled model which includes overpressure generation due to mechanical compaction and conversely the effect of the generated overpressure on the stress field.

2. The Northwest Borneo Thrust Belt

The northwest Borneo Basin has originated from a complex plate tectonic history consisting of multiple episodes of extension and compression, involving both oceanic and continental crust (Hesse et al., 2009, 2010; Ingram et al., 2004; Morley, 2009). The tectonic events relevant to the formation of the fold-and-thrust belt date from Late Miocene to present (Hesse et al., 2009; Ingram et al., 2004), which occurred due to the combined effects of plate tectonic compression and delta-related gravity driven flow, linked to updip extension (Hall & Morley, 2004; Hesse et al., 2009; Ingram et al., 2004; King et al., 2009; Morley, 2009; Morley et al., 2008; Simmons et al., 2007; Tingay et al., 2005). The thin-skinned compressional deformation originated through sediment sliding on a decollement surface located within the overpressured Setap Shale formation. The present-day accumulated shortening ranges from 8 to 13 km (Hesse et al., 2009). The thrust front strikes NE-SW with ongoing shortening toward the NW (Figure 1). The structures are quite regularly spaced with an average separation of 10 km between consecutive crests. The faults decrease in age toward the distal parts of the sediment wedge, as they approach the thrust front (Ingram et al., 2004; Morley et al., 2008). The relief of the various thrust hanging wall fault bend folds increases toward the hinterland, and many of the most deformed folds show a prominent seafloor expression (Hesse et al., 2009; Ingram et al., 2004).

The stratigraphy mostly consists of interbedded hemipelagic and pelagic shales with some turbidite fan sandstones (Ingram et al., 2004). Published log data show a high clay volume content in the shaley intervals (Couzens-Schultz & Azbel, 2014).

3. Model Setup

The numerical model is built within the finite element software Parageo (Crook, 2013). This geomechanical code allows the simulation of the coupled nature of the forward evolution of geological structures. A Lagrangian reference frame is used to describe the displacement of the solid particles (material description), whereas the displacement of the fluid phase particles is described using an Eulerian reference frame (i.e., the fluid flows through the mesh of the solid phase). The code includes critical state-based constitutive models for the simulation of the sediment rheology along with the evolution of the material properties. It is also able to model sedimentation and encompasses automated, adaptive, remeshing algorithms that enable refinement
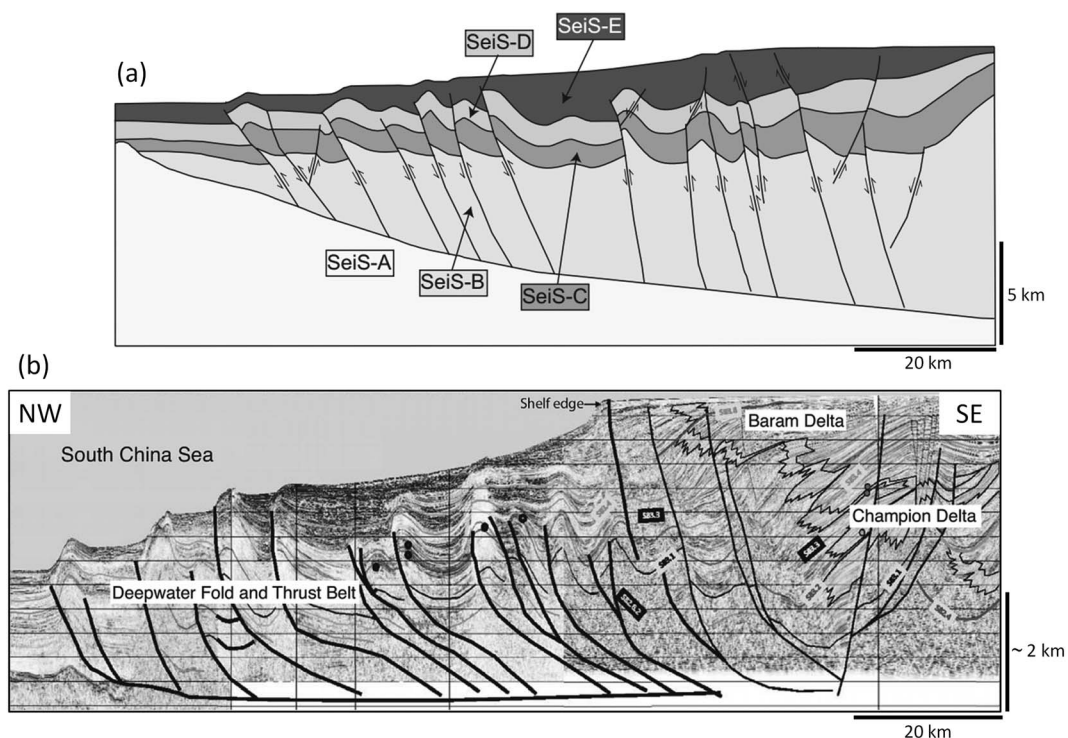
Figure 1. West Borneo thrust belt: (a) present-day interpreted seismic cross section from restoration presented by Hesse et al. (2009) and (b) interpreted seismic cross section after Couzens-Schultz and Azbel (2014).

of the mesh in the most active deforming elements while keeping the less active elements relatively coarse; this optimizes computational power. The remeshing procedure is a key feature in large strain problems and overcomes the excessive mesh distortion that would otherwise cause a premature termination in the simulation. At the same time its adaptability facilitates the proper modeling of emerging faults by refining the elements in strain localization bands. The code also encompasses an energy regularization strategy to handle mesh size dependency of strain localization.

3.1. Geometry and Boundary Conditions

The twin aims of this study are to model overpressure development in a fold-and-thrust belt and to explore the significance of fluid pressure for structural evolution. The model considers the various and complex, coupled interactions between sediment deposition, lateral shortening, fault initiation/offset, mechanical compaction, overpressure generation, and fluid flow.

We constrain and validate the model using published data from the NW Borneo thrust. The initial model geometry (Figure 2) is defined according to the restoration presented by Hesse et al. (2009). The sediment present at initialization consists of an assumed overconsolidated, 45 km long shale wedge with a basal slope of 0.04, a surface slope of 0.02, and a maximum height of 4.3 km. The basal boundary is divided by a fault discontinuity boundary condition. A prescribed displacement is assigned to both the right-hand boundary and the basal boundary to the right of the fault discontinuity, in such a way that the shortening is mainly accommodated on the fault discontinuity. Vertical and horizontal motions are prevented at the basal boundary to the left of the fault discontinuity, and horizontal motion is prevented at the left lateral boundary. The initial stresses are considered geostatic with an effective stress ratio of $K_0 = 0.8$.

The sedimentation of five additional clay layers corresponding to seismic units C, D, and E in Hesse et al. (2009) is modeled synchronous to shortening. The five sedimentation horizons are defined according to the calculated decompacted thickness at a reference porosity of each seismic unit in the thrust front location, assuming hydrostatic pressures and accounting for differential sediment deposition along the model length.

From the restoration by Hesse et al. (2009), which refers to the reverse modeling of geometry evolution in order to infer the past configuration of structures, we infer fault offsets ranging from 0.25 to 1.94 km measured at the oldest horizon (top of seismic unit B). We prescribe the amount of total displacement to predict a fault
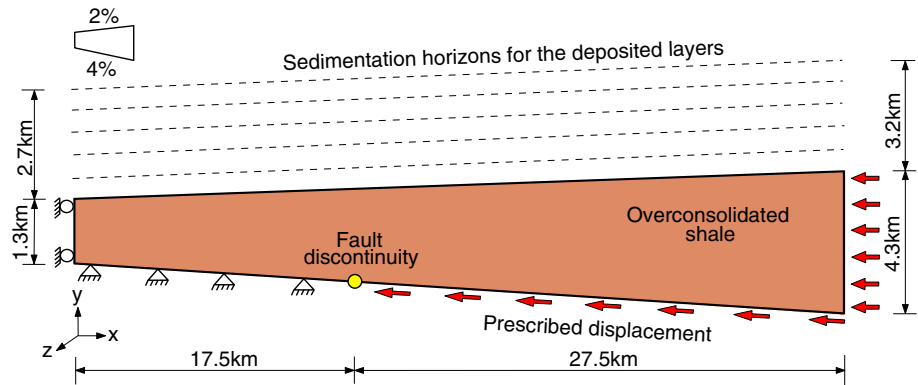
Figure 2. Schematic representation of the model setup. The initial shale wedge is assumed to be overconsolidated so that the thrust fault can arise naturally from the prediction of the constitutive model and the imposed boundary conditions. Five additional layers are deposited during the shortening event. The figure shows the coordinate system used in this paper, in which *x* is the in-plane horizontal direction, *y* is the vertical direction, and *z* is the out-of-plane direction perpendicular to the plane of deformation.

offset which is on the upper bound of the measurements (the required horizontal displacement is 3 km). The transient shortening rate is defined according to the normalized fault offset as a function of time inferred from the thrust fault in the restoration located in the most foreland location (the calculated average shortening rate is 566 m/Ma).

The bottom and lateral boundaries are prescribed as nonflow boundaries. It should be noted that this assumption will have no measurable effect on the model results as the lateral boundaries are remote and no high permeability layers are considered. The prescribed pressure at the surface is given by a rising water level, which ensures that the sediments are always saturated and in deep water conditions.

3.2. Material Model

The constitutive model presented here is based on the decomposition of the effective stress tensor, σ', into deviatoric and volumetric parts (Terzaghi, 1923):

$$\sigma' = s + p'I \quad \text{with} \quad p' = \frac{1}{3}\text{tr}[\sigma'] \tag{1}$$

where p' denotes the effective mean stress, s is the deviatoric stress tensor, I is the second-rank identity tensor, and $\text{tr}[\cdot]$ is the trace operator of $[\cdot]$. In addition to the effective mean stress, the deviatoric stress $q = \sqrt{\frac{2}{3}(s : s)}$ is needed in the constitutive formulation of the yield surface and flow potential. The deviatoric stress can be written in terms of the three principal effective stresses σ'_1, σ'_2, and σ'_3 as $q = \sqrt{\frac{1}{2}\left[(\sigma'_1 - \sigma'_2)^2 + (\sigma'_1 - \sigma'_3)^2 + (\sigma'_2 - \sigma'_3)^2\right]}$. It may be noted that for sediments buried under uniaxial strain conditions (i.e., $\sigma'_2 = \sigma'_3$) our definition of deviatoric stress, widely adopted in critical state soil mechanics, coincides with the definition of differential stress used in geophysics and structural geology literature ($q = \sigma'_1 - \sigma'_3$).

3.2.1. Yield Surface

The sediment rheology for the shale and clay-rich lithologies is modeled by means of the Soft Rock 4 (SR4) constitutive model which is based on typical implementations of the Cam Clay model (e.g., Wood, 1990). The SR4 model was chosen to simulate mudrock rheology as it allows modeling of both mudrock compaction and faulting depending on the evolution of the stress state relative to the yield surface. Furthermore, the SR4 parameters allow flexibility in defining the shape of the yield surface rather than relying on an elliptical yield surface as in the classical Modified Cam Clay model, which overestimates the strength in shear (Roscoe & Burland, 1968). The SR4 is a poroelastoplastic, rate-independent, nonassociative critical state constitutive model. The SR4 yield surface, which encloses the region of elastic stresses, is representative of the material strength (Figure 3a). When stress paths intersect the yield surface, plastic deformations are produced, whereas stress paths moving inside the yield surface result in elastic strains. The SR4 yield surface is composed of two different surfaces that intersect in a continuous manner at the peak stress. The cap side, where compaction
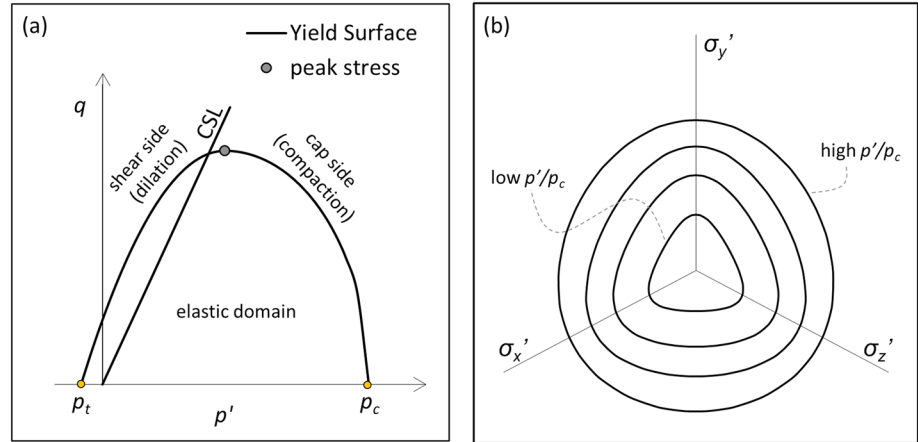
Figure 3. (a) Yield surface in the p'-q plane. Yielding on the cap side (to the right of the intersection of the critical state line (CSL) with the yield surface) would cause compaction (volume reduction). Yielding on the shear side (to the left of the intersection of the CSL with the yield surface) would cause dilation (volumetric increase). (b) Yield surface in the deviatoric plane for various values of p'. The σ'_x, σ'_y, and σ'_z are the effective stresses in the in-plane horizontal and vertical directions and the out-of-plane horizontal direction, respectively.

is expected to take place, is defined by the Modified Cam Clay surface, whereas the shear side is defined by means of the Soft Rock 3 (SR3) constitutive model's surface (Albertz & Lingrey, 2012; Albertz & Sanz, 2012):

$$\phi(p', \varepsilon_v^p) = g(\theta, p')q + (p' - p_t) \tan \beta \left[\frac{(p' - p_c)}{(p_t - p_c)} \right]^{1/n} \tag{2}$$

for $p' \geq p_{\phi_{\text{peak}}}$ and

$$\phi(p', \varepsilon_v^p) = \left[g(\theta, p') \right]^2 q^2 - M_\phi^2 p_{\phi_{\text{peak}}}^2 \left[1 - \frac{(p_{\phi_{\text{peak}}} - p')^2}{(p_{\phi_{\text{peak}}} - p_c)^2} \right] \tag{3}$$

for $p' < p_{\phi_{\text{peak}}}$

where p_t is the tensile intercept of the yield surface with the hydrostatic axis, p_c is the preconsolidation pressure or compressive intercept of the yield surface with the hydrostatic axis, $p_{\phi_{\text{peak}}}$ is the effective mean stress at q peak value, ε_v^p is the plastic volumetric strain, M_ϕ is the slope of the line that intersects both the origin of the p'-q space, and the yield surface in q peak value, β and n, are material constants which define the shape of the yield surface in the p'-q plane and $g(\theta, p')$ is a function that controls the rounded triangular shape of the yield surface in the deviatoric plane (plane normal to hydrostatic axis as seen in Figure 3b) to account for different strengths in compression and extension. Lode's angle θ can be related to σ'_1, σ'_2, and σ'_3 as

$$-\frac{\pi}{6} \leq \theta = \tan^{-1} \left[\frac{1}{\sqrt{3}} \left(\frac{2\sigma'_3 - \sigma'_1 - \sigma'_2}{\sigma'_1 - \sigma'_2} \right) \right] \leq \frac{\pi}{6} \tag{4}$$

3.2.2. Flow Potential

The model formulation allows for the definition of the flow rule in such a way that the critical state (i.e., continuous shear at constant volume) is located on the shear side of the yield surface, which is consistent with experimental observations on clays (Cotecchia & Chandler, 1997; Ventouras & Coop, 2009). Yielding on the right-hand side of the critical state (cap side) will result in volumetric reduction and strength increase (hardening) leading to diffuse plastic strain, whereas yielding on the left-hand side of the critical state (shear side) will be accompanied by volumetric increase and strength decrease (softening), leading to plastic strain localization, analogous to faulting. The flow potential surface is defined as

$$\psi(p', \varepsilon_v^p) = q + (p' - p_t) \tan \psi \left[\frac{(p' - p_c)}{(p_t - p_c)} \right]^{(1/m)} \tag{5}$$

for $p' \geq p_{\psi_{\text{peak}}}$ and

$$\psi(p', \varepsilon_v^p) = q^2 - M^2 p_{\psi_{\text{peak}}}^2 \left[1 - \frac{(p_{\psi_{\text{peak}}} - p')^2}{(p_{\psi_{\text{peak}}} - p_c)^2} \right] \tag{6}$$

for $p' < p_{\psi_{\text{peak}}}$

Table 1
Material Parameters for the SR4 Model for Clay (Syntectonic Sediments) and Shale (Preexisting Sediment Wedge) Lithologies

Parameter	Symbol	Units	Value
Initial preconsolidation pressure	p_{c0}	MPa	0.1
Initial tensile intercept	p_{t0}	MPa	−0.003
Friction parameter	β	deg	62
Friction exponent	n	–	1
Dilation parameter	ψ	deg	66.3
Dilation exponent	m	–	0.8
Deviatoric plane correction exponent	N^{π}	–	0.25
Deviatoric plane shape correction parameter	β_0^{π}	–	0.6
Deviatoric plane shape correction parameter	β_1^{π}	–	0.6
Grain density	g_s	kg/m^3	2,700
Reference porosity at deposition	Φ_0	–	0.555
Bulk modulus at deposition	K_s	MPa	10
Slope of the isotropic compression line in in the e-ln p' plane	λ	–	Determined from the hardening law curve
Slope of the unloading line in the e-ln p' plane	κ	–	0.02
Poisson's ratio	ν	–	0.3

Note. The parameters that define the shape of the yield surface have been defined to obtain a residual friction angle of about 26°, which is a reasonable value for a mudrock lithology. The flow surface has been defined so that the critical state occurs on the shear side rather than at the peak stress, which agrees with the experimental data on clays (e.g., Cotecchia & Chandler, 1997; Ventouras & Coop, 2009). The parameters for porosity and isotropic compression line have been obtained from the density data (Couzens-Schultz & Azbel, 2014). The remaining material parameters have been estimated based on engineering judgment.

where M is the slope of the critical state line, $p_{\psi_{peak}}$ is the effective mean stress corresponding to the peak value of q for the flow potential surface, and ψ and m are material constants which define the shape of the flow potential surface in the p'-q plane. Note that the flow potential surface does not have any deviatoric correction term (as opposed to the yield surface) as it is circular in the deviatoric plane for all values of p_c. For more details on the model equations of the SR4 the reader is referred to Obradors-Prats et al. (2016).

3.2.3. Material Parameters

Constitutive model parameters (Table 1) were defined to be representative of clay/shale lithologies, and homogeneous material properties were assigned to each of the five syntectonic layers, at deposition. During the simulations, properties such as porosity and strength update as a function of compaction; nevertheless, in these idealized models, the effect of the mechanical stratigraphy due to the presence of sandstone layers is neglected. This assumption was adopted as a necessity due to the geomechanical modeling requirements and the flow behavior of sandstones: on one hand the geomechanical model should be long enough to min-imize boundary effects in the area of interest, and, on the other hand, the incorporation of high permeability sandstone layers would result in the transfer of overpressure away from the main structures toward the lateral boundaries. However, this assumption is reasonable as the sands in NW Borneo are mostly turbidite channels and discontinuous fans that are surrounded by mudrocks (Ingram et al., 2004).

The hardening law which defines the clay compressibility (or in other words, the strength evolution with porosity) is defined according to a normal compaction trend (NCT) that describes the porosity distribution with depth in normally pressured sediments. Values were obtained from published density data from the NW Borneo thrust belt (Couzens-Schultz & Azbel, 2014), assuming that the sediments are normally pressured (Figure 4a). The initial shale wedge is assumed to be overconsolidated (i.e., the preconsolidation pressure is higher than the initial effective mean stress after model initialization) in order to ensure that the stress path meets the yield surface on the shear side. This is a requirement for modeling brittle deformation,
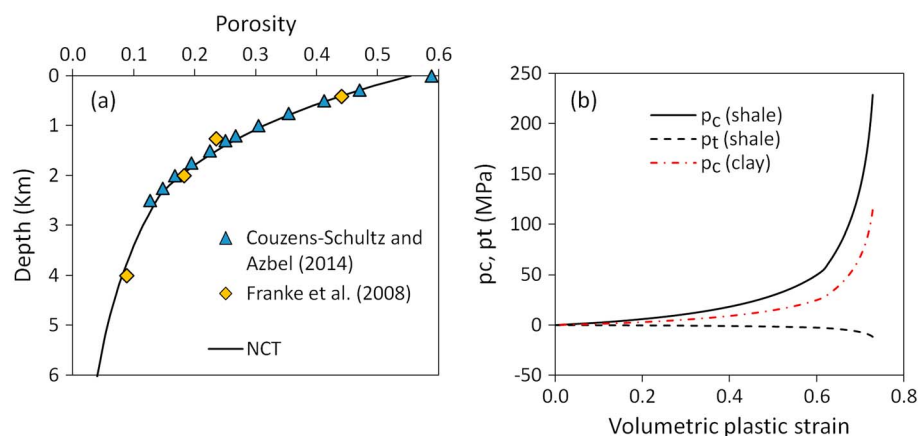
Figure 4. (a) Normal compaction trend (NCT) derived from published density data from Couzens-Schultz and Azbel (2014) for the NW Borneo thrust belt drape sediments, assuming hydrostatic pressures, a matrix density of 2,650 kg/m^3, and water density of 1,000 kg/m^3. The data from Franke et al. (2008) correspond to the density values from Table 2 in their paper, with the depth estimated as the middle depth point for seismic units B, C, D, and E at a selected location near the thrust front in Figure 1a. (b) Hardening law curves for clay (syntectonic sediments) and shale (preexisting sediment wedge) derived from the NCT. The shale to clay p_c ratio for a given value of volumetric plastic strain is 2.6. The clay p_t has a constant value close to 0 and therefore is not shown.

which is a type of plastic deformation that can be predicted with Cam Clay-type models resulting in rapidly strain-softening materials and leading to localization phenomena with high displacement gradients in narrow regions of intense plastic strain. The appropriate overconsolidation ratio required for faulting has been determined by means of a sensitivity analysis. It should be emphasized however that this material assumption does not necessarily honor the consolidation state of the sediments in NW Borneo. It is a challenge to estimate parameters such as preconsolidation pressure without any geomechanical test data, and this assumption is made based on engineering judgment in order to predict the desired deformation style in the model.

After the model initialization, the initial porosity prescribed at the top horizon of the shale wedge is 0.14 (i.e., the porosity at 2.4 km depth in the NCT) and decreases with depth following the NCT. The permeability is a function of porosity and is updated according to the amount of compaction and dilation. The model developed by Yang and Aplin (2010) is used to estimate the permeability-porosity relationship as a function of clay fraction. This fraction was calibrated according to pore pressure data from the NW Borneo thrust, assuming that the sandstones from which pore pressure data were taken are in equilibrium with adjacent shales and that the measurements were performed at the maximum overpressured location. By doing this, we ensure that the conditions for hydraulic fracturing are not reached in any location of the model, thus preventing unwanted termination of the simulation (Figure 5).

3.3. Mesh
The finite element mesh of the model consists of approximately 14,000 unstructured triangular elements (initial configuration) to approximately 78,500 elements (final configuration after sedimentation and adaptation to accommodate strain localization). The initial element length for the shale wedge is 150 m. An adaptive remeshing approach is adopted, which progressively decreases the element size as a function of plastic strain, up to a minimum element length of 40 m. This procedure facilitates a proper capture of strain localization. For the mesh of the deposited layers, the element length is fixed at 80 m to ensure an optimum balance between model resolution and computational time.

4. Results and Discussion
4.1. Structural Development
The structural development predicted by the model is presented in Figure 6. During the early stages of deformation a box fold bounded by two kink bands develops within the overconsolidated shale, initiating from the basal discontinuity and terminating on the contact with the first deposited layer. A wide anticline starts to develop within the syntectonic sediments, with a systematic sediment onlap on the older layers due to synchronous sedimentation and thrust-related uplift (Figure 6a). With further shortening the offset in the principal, foreland-dipping thrust increases. The conjugate kink band is carried forward along the principal thrust,
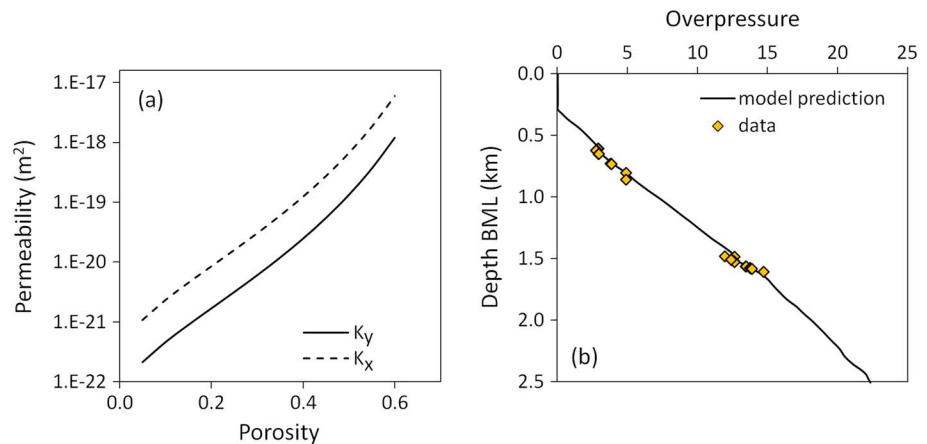
Figure 5. (a) Porosity-permeability relationships for the clay (syntectonic sediments) and shale (preexisting sediment wedge) lithologies. k_x and k_y are the permeabilities in the direction parallel and perpendicular to the bedding plane, respectively. The permeability in the direction perpendicular to the bedding plane was obtained using Yang and Aplin (2010) model for a clay fraction of 0.73. The permeability in the direction parallel to the bedding plane was obtained assuming transverse anisotropy with an anisotropic ratio of $k_x/k_y = 5$. (b) Comparison of model predictions and field measurements of overpressure (fluid pressure in excess of hydrostatic pressure).

and new, closely spaced kink bands develop, dipping hinterland (Figure 6b). At the end of the deformation (Figure 6c) the predicted structure consists of a fold propagation thrust dipping in the shortening direction, with six kink bands dipping in the opposite direction to the principal thrust. A wide, nonsymmetric anticline has been formed in the syntectonic sediments. The principal thrust fault offset is between 1.7 and 1.8 km (Figure 7a) which is within the upper bound of the observed faults offsets in the restoration by Hesse et al. (2009). The maximum uplift experienced in the thrust hanging wall is 1.39 km, which facilitated the formation of the anticline in the syntectonic sediments (Figure 7b).

It is clear that there is a contrast between the mechanical behavior of the overconsolidated shale and the overlying sediments. Plastic strain is localized within the overconsolidated shale, whereas the overlying sediments
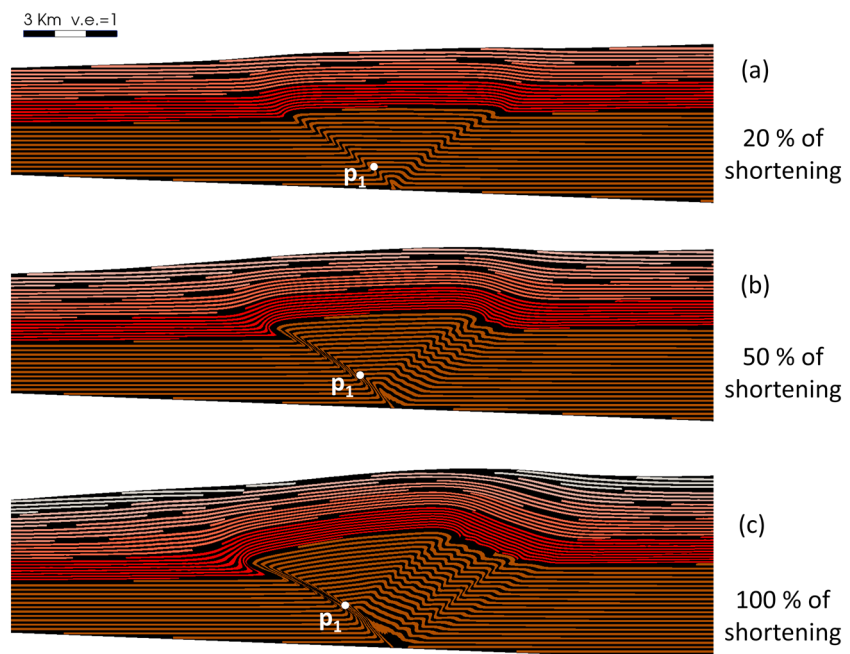

Figure 6. Model material grid at (a) 20%, (b) 50%, and (c) 100% of shortening. The brown grid corresponds to the initial overconsolidated shale wedge. The grid that covers colors from red to white corresponds to the five deposited layers during the shortening. p_1 indicates the position of a tracked material point.
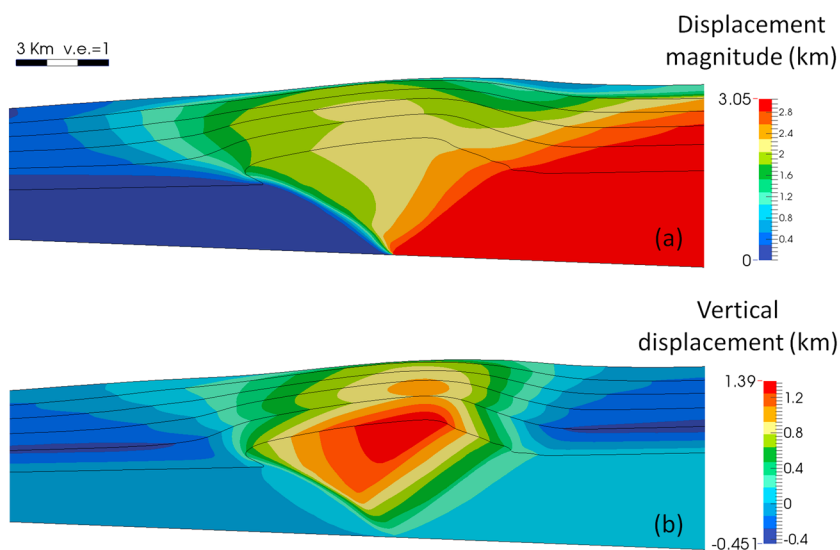
Figure 7. Total (a) displacement magnitude and (b) vertical displacement at the end of the shortening. Positive values in vertical displacement correspond to upward movement, whereas the negative values stand for downward movement. The discontinuous displacement field within the shale wedge is consistent with faulting.

show a much more diffuse, plastic shear strain distribution (Figure 8). The fault has not propagated within the syntectonic formations and dies at the top of the shale wedge. This behavior occurs because the model is limited to consideration of the mechanical aspects of compaction only; other mechanisms that might contribute to sediment consolidation (e.g., diagenetic and chemical effects, and creep), with the consequent increase in sediment strength, have been neglected. As a consequence all the sediments deposited during the simulation can only be underconsolidated (or normally consolidated once excess pore pressure is dissipated) and can therefore only deform in a ductile manner. It should be recalled that a prerequisite to predict brittle faulting using critical state-based constitutive models is that the stress path should meet the yield surface on the shear side (illustrated in section 4.3). For the current application, where overpressure develops synchronous to the deposition of sediments, the prediction of brittle faulting within the deposited sediments using a critical state model would only be possible if processes other than mechanical compaction increase the sediment strength, leading to an apparent overconsolidated state.

In natural basins, sediments are usually altered by both mechanical and nonmechanical processes. During burial they develop structure and anisotropy and can experience changes due to chemical reactions even at shallow depths, such as early carbonate cementation and the transformation from Opal A to Opal CT (Ishii et al., 2011). Nonmechanical processes might increase sediment strength, resulting in an apparent overconsolidation and exerting a first-order control on rheology and thus on macrostructural development. This has been explored by Roberts et al. (2015), who used geomechanical models to show how diagenetic effects might trigger brittle deformation and formation of polygonal fault systems within diatomaceous mudstones in passive tectonic settings. Therefore, we believe that when the goal is to simulate the structural evolution of a
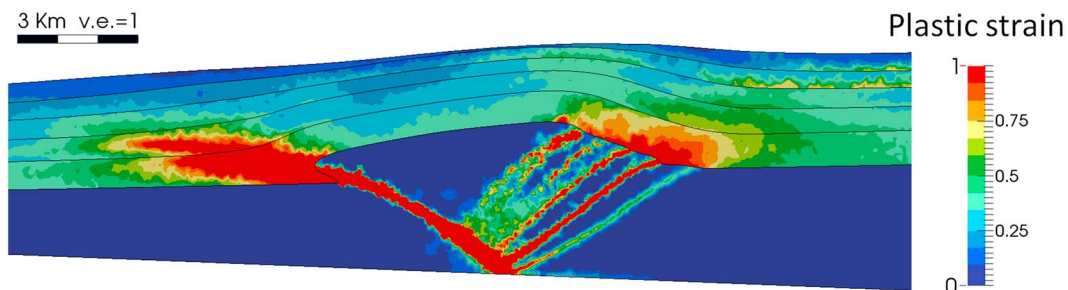

Figure 8. Plastic shear strain at the end of the shortening. The range has been arbitrarily limited from 0 to 1 (0% to 100% of strain) so all the structures are clearly visible, but the maximum nodal value at the basal discontinuity is 14.6.

geological system that accounts for sedimentation, the incorporation of nonmechanical compaction and diagenetic effects within geomechanical models becomes crucial in order to capture the appropriate structural features. As mentioned earlier, however, nonmechanical compaction effects are not currently included in our simulations. It should be noted that in the case of NW Borneo sediments, the analysis of cuttings samples on multiple wells has shown little evidence of diagenetic processes that would have strengthened the rock. The compaction trend, however, suggests that additional porosity loss has occurred relative to typical short-term K_0 experiments on clays. This would change the prekinematic stress state relative to the yield surface and also may have resulted in increased strength or apparent overconsolidation.

4.2. Comparison With Field Structures

According to Hesse et al. (2010) folds in the deepwater Sabah NW Borneo region can be classified into four types. Structural features that differ between those four fold types consist of the presence or absence of seafloor expression, the presence or absence of normal faults in the anticline crest, the shape and angle of the thrust fault, the forelimb and backlimb dipping angles, the interlimb angle, the preservation or the partial erosion of the fold crest, and the presence or absence of an overlying overburden.

The structure predicted by the model has a smooth seafloor expression with a lack of normal faults on the crest, due to the ductile behavior exhibited by the syntectonic sediments. Similar to the results reported in Hesse et al. (2010), the structural angles measured from the top horizon of the first sedimented layer (prekinematic layer) consist of a forelimb dip of 22°, a backlimb dip of 20°, and an interlimb angle of 138°. The thrust fault is curved (in a fashion similar to Figure 9 in Hesse et al. (2010), with a progressive decrease in the dip angle from 44° on the basement to 13° in the intersection with the first sedimented layer, where the ramp becomes a blind fault. Overall, the predicted structure captured some of the first-order elements of the type-II and type-III anticline descriptions. In Hesse et al. (2010) type-II anticlines are described as structures having a clear seafloor expression, an internally faulted crest, basinward vergence, an interlimb angle between 140° and 170°, steep forelimbs with dip angles between 10° and 20°, and backlimbs with average angles of 13°. Type-III anticlines (most common type in NW Borneo) exhibit a clear seafloor expression, are affected by crestal normal faulting, show mass movement on their flanks, have an average interlimb angle of 135°, are often underlain by slightly curved thrust faults with dip angles between 40° and 50° that terminate as a blind thrust, and have steep forelimbs with average dipping angles of 25° and backlimbs that dip an average of 20°.

However, there are clear differences between the predicted structure and the published field data: the lack of fault propagation within syntectonic sediments, the lack of normal faults in the anticline crest, and the presence of six kink bands dipping basinward in the prekinematic sediments.

Dissimilarities in structural features might be partly explained by the lack of diagenetic effects in the model (and the consequent required material assumptions, e.g., the grade of initial overconsolidation of the prekinematic shale wedge). They might also be attributed to the simplification in the model architecture as opposed to the greater complexity of the field geology, including the role of mechanical stratigraphy, the heterogeneity of geomechanical properties, and the variations in the stress tensor produced by the adjacent thrust faults.

4.3. Influence of Overpressure on Structural Development

Structural style in shortening environments depends on numerous factors such as sediment strength, stress state, the existence of weak planes, sediment deposition, and the pore pressure regime (Albertz & Lingrey, 2012; Albertz & Sanz, 2012; Thornton & Crook, 2014). For example, Hubbert and Rubey (1959) provide a mechanical explanation for the role of overpressure in overthrust faulting in which high overpressures decrease the effective stresses in detachments and, consequently, also decreases the frictional resistance, facilitating the slide of large masses of sediment. Furthermore, experimental observations on clays and shales show that the style of internal deformation at the laboratory scale depends on effective stress, where low effective stress favors strain localization and brittle deformation (Nygård et al., 2006).

In order to test the influence of overpressure on the predicted structural style within critical state, coupled geomechanical models, we performed a drained analysis in which pore pressure is kept hydrostatic during the entire simulation. The results show that the predicted structure at the present day consists of a wide anticlinal fold with onlap of the syntectonic sediments in the older layers (Figure 9). Clear differences can be observed relative to the results from the coupled model (Figure 6c), with neither fault offset nor kink bands predicted. Compared to the drained analysis, overpressure generation in the coupled analysis results in a
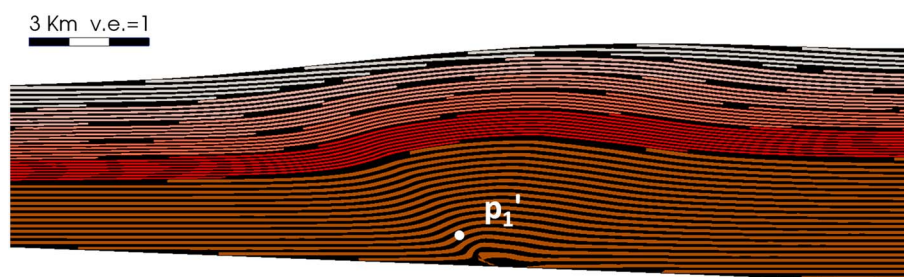
Figure 9. Predicted structure under drained conditions (hydrostatic pore pressure) at the end of the shortening. p_1' indicates the final position of a tracked material point.

relatively low shortening-induced increment in the effective mean stress; the magnitude of the shortening-induced increase in the total horizontal stress translates into an increase in both overpressure and horizontal effective stress.

In addition, the increase in overpressure leads to a decrease in the vertical effective stress. Consequently, the stress path in the p'-q space is sharp, with a high q/p' ratio increment. This results in the stress path intersecting the initial yield surface on the shear side (to the left of the critical state), resulting in strain softening and strength decrease in the fault sediments (Figure 10a). The deformation is localized, forming a plane of weakness which is the continuum equivalent of a fault, so that the subsequent shortening is accommodated by sliding on this fault. On the other hand, the dissipation of overpressure in the drained analysis facilitates development of higher effective mean stress, as all the increase in the total horizontal stress translates into an increase in the horizontal effective stress. In addition, as the pore pressure remains hydrostatic, the vertical effective stress remains practically unchanged, whereas the deviatoric stress is independent of the pore pressure. Consequently, the stress path in p'-q space has a lower q/p' ratio increment relative to the coupled analysis and the stress path intercepts the yield surface on the cap side (to the right of the critical state). Consequently, there is strain hardening and strength increase within a ductile deformation regime (Figure 10b).

Our modeling results agree with classical rock mechanics theory, which by means of failure criteria such as the Mohr-Coulomb criterion, establish the stress conditions that lead to failure. In that context the reduction of the effective stresses (e.g., because an increase in overpressure) might promote fracturing and faulting by lowering the frictional shear resistance of the rock (Einstein & Dershowitz, 1990; Hubbert & Rubey, 1959; Sibson, 2003).

The contrast in the predicted deformation style between the coupled and drained models is highly dependent on the initial state of consolidation. For higher degrees of overconsolidation (higher OCR) a thrust fault may also be predicted at drained conditions. We recall that the initial preconsolidation pressure for the overconsolidated preexisting shale wedge was defined by determining the minimum OCR required to predict a thrust fault in the coupled analysis. The relative roles of overpressure and consolidation state on the mode of
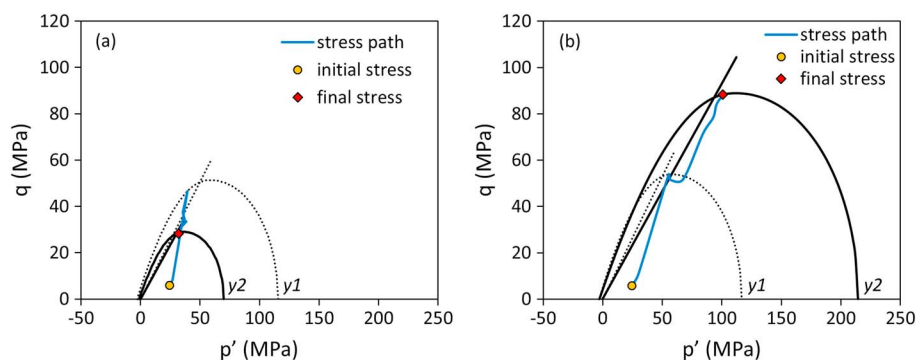

Figure 10. Stress paths for points p_1 (a) and p_1' (b) shown in Figures 5c and 8, respectively. y1 and y2 indicate the initial and final yield surfaces, respectively. Note that the initial coordinates for both points are identical, whereas the final coordinates differ due to the displacement regimes resulting from the different structural styles.

deformation (ductile-brittle) have been discussed experimentally by (Bolton et al., 1998). They concluded that despite the fact that high overpressures favor low effective stresses, the timing of overpressure development is the crucial factor in determining the mode of deformation, as it controls the degree of consolidation relative to the effective stress. For example, sediment which develops early overpressure, retarding its consolidation, is likely to deform in a ductile manner when sheared. Conversely, sediment which is overpressured subsequent to consolidation is more likely to exhibit brittle deformation in shear (Bolton et al., 1998). These observations are in good agreement with our numerical results: the overpressured, overconsolidated initial shale wedge show brittle behavior, whereas the unconsolidated, overpressured, syntectonic sediments deform in a ductile manner.

The role of overpressure on structural style has been previously discussed by several authors who have recognized that high overpressures facilitate the localization of detachments within overpressured units in fold-and-thrust belts because of the resulting decrease in frictional strength (Aydin & Engelder, 2014; Bilotti & Shaw, 2005; Cobbold et al., 2009, 2004; Corredor et al., 2005; Krueger & Grant, 2011). This has also been demonstrated experimentally using sandbox models (Cobbold & Castro, 1999; Cobbold et al., 2009, 2001, 2004; Mourgues & Cobbold, 2006). Nonetheless, the localization of detachments in highly overpressured, unconsolidated shales, commonly known as mobile shales, has been often attributed to their ductility. Although this might seem contrary to our model observations, it should be noted that our model assumes an initially overconsolidated shale that forms part of the wedge, not the detachment itself, and the focus here is upon the internal deformation style. Moreover, Maloney et al. (2010) reinterpreted the internal mechanisms of shale deformation in the south of Niger Delta thrust belt detachment, located within the overpressured Akata formation, and argued that brittle processes might also be involved within the so-called ductile detachments.

Analog sandbox modeling experiments (Cobbold et al., 2001; Mourgues & Cobbold, 2006) have been used to investigate how different degrees of overpressure influence the predicted structural style and internal deformation in thrust wedges. Cobbold et al. (2001) concluded that deformation style is highly influenced by the level of overpressure. Models with pore pressures approaching the lithostatic stress exhibit relatively low and long structures with large displacement accumulating in the frontal forethrust and relatively low surface slope angle. In contrast, experiments conducted at low overpressures exhibit higher and shorter structures with higher slope angles. In addition, fewer backthrusts were developed in low overpressure experiments compared to those with high overpressure (e.g., comparison of A2 and A6 experiments in their paper). Mourgues and Cobbold (2006) showed that in their experiments, high overpressures favored ductility, which might also seem contrary to our modeling results. However, direct comparison between our numerical models and these experimental observations is not straightforward due to differences in (1) the model scale, fluid viscosity, and velocity; (2) the origin of the overpressure, that is, prescribed rather than arising from sediment deformation; (3) boundary conditions—whereas the experiments were performed on an horizontal, homogeneously frictional base, our model's basal boundary is tilted and includes a discontinuity as a trigger for the thrust fault; and (4) sand deformation in sandbox experiment conditions is dominated by friction so that they behave in a brittle manner even at zero pore pressure conditions (e.g., see the kink bands stacked nearby the piston in Figure 9a from their paper). Consequently, the basal overpressure contributes to the propagation of the brittle deformation away from the piston in the experiments (e.g., see Figure 9b from their paper for comparison). For the case of overpressures approaching the lithostatic, failure conditions are relatively easy to achieve because of the reduction in strength. This facilitates a more distributed brittle deformation across the domain (e.g., see Figure 9c from Mourgues and Cobbold (2006), as the formation of new kink bands eventually requires less energy than uplifting the sand by shear on the previously created kink bands. We do not, therefore, interpret this as an increase in ductility relative to the case with zero pore pressure but a brittle deformation with a different structural style.

To corroborate this statement, a setting similar to the sandbox C series in Cobbold et al. (2001) has been simulated. The initial geometry of the model consists of a high permeability sand basal layer of 1 cm height overlain by a succession of three 1 cm high and 30 cm long layers consisting of a low permeability loess layer and two high permeability sand layers, respectively. The three-layer succession is pushed toward the left by a rigid piston with a friction contact surface defined on the interface. The material properties were defined according to the properties described in Cobbold et al. (2001), and the pore fluid was defined with air properties to be consistent with the experiments. Two cases were simulated; one with "dry" conditions (no pore fluid pressure) and one with a prescribed pore pressure of 4.5 cm of hydrostatic head at the basal boundary.
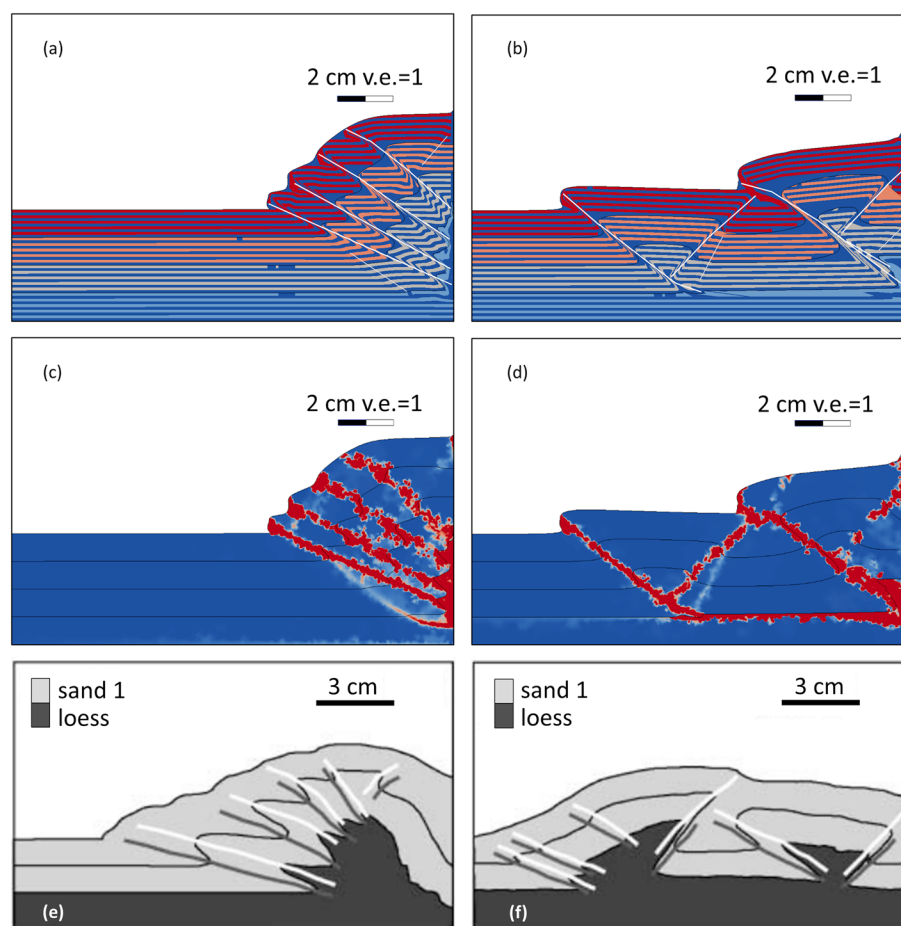
Figure 11. (a–d) Numerical simulation results of a thrust sandbox experiment and experimental results (e) for C1 and (f) C2 setups from Cobbold et al. (2001). Figures 11a, 11c, and 11e correspond to dry setups, and Figures 11b, 11d, and 11f correspond to setups with a basal pore fluid pressure of 4.5 cm of hydrostatic head. The experimental captions show the structural configuration after 10 cm of horizontal displacement, whereas the shown numerical results are obtained after 5.33 cm of horizontal displacement (the simulation for the dry case terminated prematurely at that time due to a geometrical issue with the basal layer dragged by the moving wall. However, the amount of displacement is sufficient to observe the effects of overpressure in the predicted structural style and compare the observations with the experimental results). Figures 11a and 11b show the material grid for the dry and overpressured cases, respectively, with thick white lines indicating the trace of the well-developed faults and the thin white lines indicating the trace of incipient faults; Figures 11c and 11d show the effective plastic strain contours with a range from 0 to 1 for the dry and overpressured cases, respectively; and Figures 11e and 11f show the structural style for the dry and overpressured cases, respectively. The dark gray and white lines in Figures 11e and 11f correspond to interpolated fault traces for the footwall and hanging wall, respectively. It can be observed how the numerical models successfully predicted the first-order structural features of the experimental settings for the two pore pressure conditions (i.e., the models predict a relatively narrow and high structure for the dry case compared to the case with basal overpressure, which predicted a shorter and longer structure resulting from the higher forward propagation of the brittle deformation).

Comparison of the predicted and experimental results (Figure 11) show that our numerical results successfully predict the change in deformation style observed in the experiments. The dry case predicts a structure consisting in a relatively short and high plateau uplifted by four stacked forethrusts with an incipient backthrust on top and an incipient forethrust rooted in the basal layer. Conversely, deformation in the basal pore pressure case exhibits faults that propagate away from the piston with a resulting predicted structure which is relatively long and low. Two forethrusts and two backthrusts delimit two box anticlinal fold structures separated by a syncline. Two incipient backthrusts are apparent, each located to the right of the major backthrusts.

It is apparent from Figure 12 that the basal pressure in the overpressured case decreased the minimum value of the effective stress at the basal layer/loess layer interface (i.e., 3 cm depth). Consequently, only a small increment in shear stress is required to achieve failure at that location. This facilitates the development of a
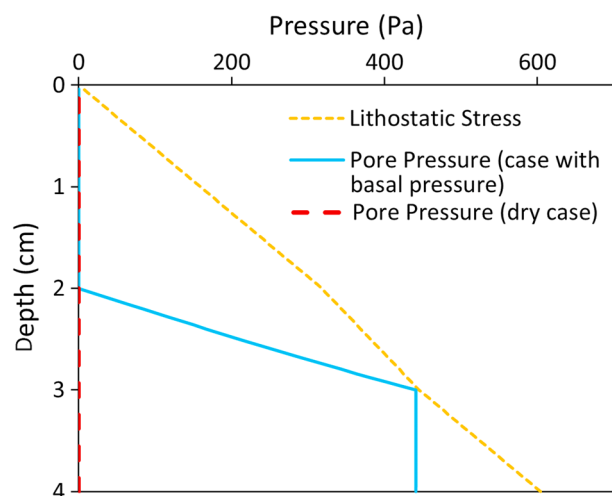
Figure 12. Pore pressure and lithostatic profiles with depth from dry and overpressured numerical sandbox models.

detachment and the forward propagation of the brittle deformation away from the piston. Conversely, the effective stress in the dry case is much higher and equal to the lithostatic. Consequently, brittle deformation develops near the moving piston.

In summary, it has been found that together with the consolidation state, overpressure plays a major role in conditioning the structural style development at both laboratory and field scales. Our numerical models have successfully captured that influence and predicted structures which are in agreement with field and experimental observations.

4.4. Stresses, Porosity, and Overpressure in Syntectonic Sediments

A key aim of this paper is to analyze the development of stresses, porosity, and overpressure in mudstones since their deposition in the thrust. The following section will therefore focus on the syntectonic sediments. The effective mean stress in the syntectonic sediments indicates a generally high overpressure regime (Figure 13a). In particular, low effective mean stresses are found in the forelimb. In contrast, the sediments deposited over the hanging wall of the thrust have a relatively high effective mean stress compared to sediments at a similar depth in other structural locations. The highest values are found in the deepest sections of the backlimb and in the sediments in contact with the thrust fault tip. High values of deviatoric stress concentrate near the thrust fault and the tips of kink bands (Figure 13b). The maximum deviatoric stress is located in the thrust fault tip where it reaches a magnitude of 10 MPa.

Two zones with high effective stress ratios are predicted in the forelimb and backlimb sediments, with values as high as 2.6 (Figure 13c). In these zones the horizontal effective stress dominates the vertical effective stress at the present day and will henceforth be called laterally compressive regions. Between these zones, near to
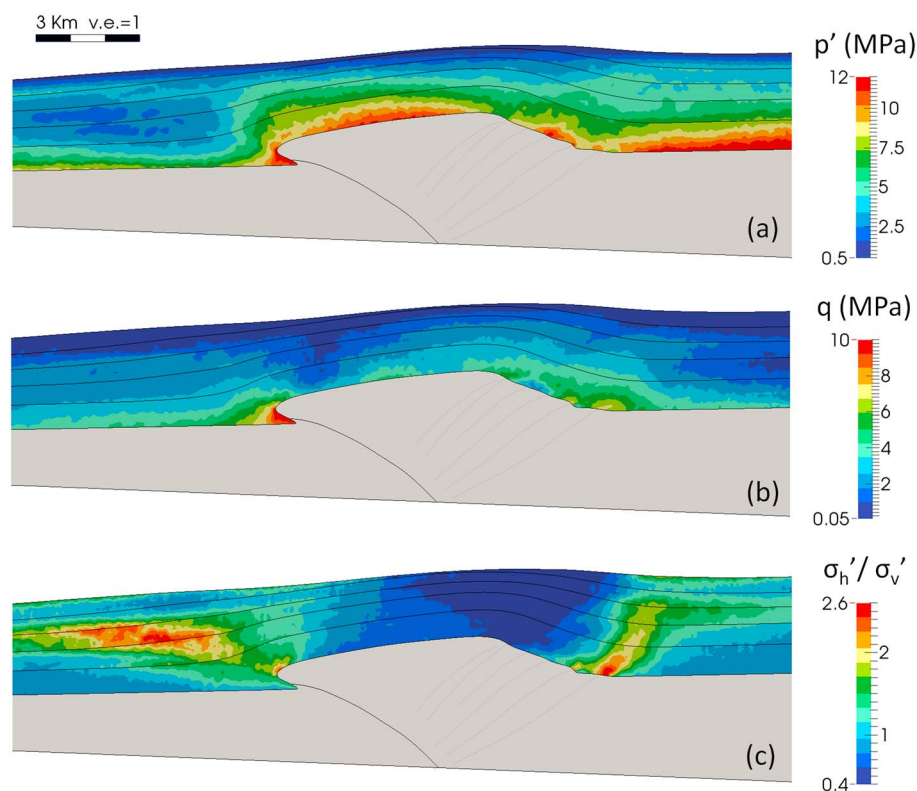

Figure 13. (a) Effective mean stress, (b) deviatoric stress, and (c) effective stress ratio in the syntectonic sediments at present day.
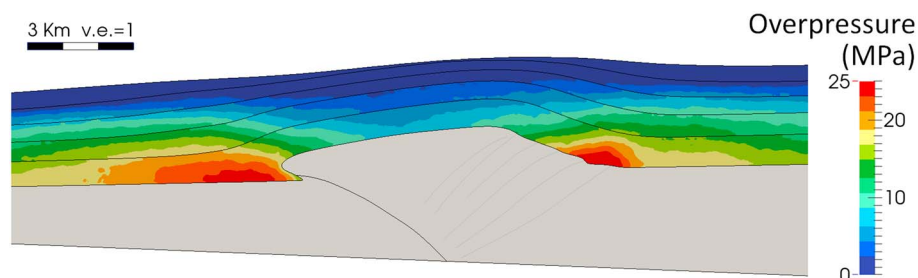
Figure 14. Overpressure distribution in the syntectonic sediments at present day.

the axial plane of the anticline, the effective stress ratio values are below the uniaxial burial effective stress ratio (also termed K_0). This zone will now be referred to as the laterally extensional region.

The overpressure in the syntectonic sediments is generally high. Pore pressure has increased above the hydrostatic values due to disequilibrium compaction related to two processes: ineffective dewatering as vertical stress increases during burial and also as a result of tectonic compressive deformation. It can be seen that two main zones of high overpressure have developed in the forelimb and backlimb, coinciding with laterally compressional regions (Figure 14). This indicates that tectonic stress has played a role in increasing overpressure, as a result of compaction, driven by tectonic strain, and the linked development of low permeability sediments, hindering dewatering. The maximum overpressure is located in the backlimb, next to the youngest kink band, and reaches 25.6 MPa in magnitude. The uplifted sediments above the thrust's hanging wall show an overpressure gradient with depth which is notably lower than the gradient in the laterally compressional locations.

The forelimb sediments show greater porosity preservation with depth than the sediments in the thrust hanging wall and backlimb locations (Figure 15). However, the large strain in sediments near to the thrust fault tip promoted a high local porosity loss, reaching porosity values of 0.14. The sediments above the thrust hanging wall have relatively low porosities compared to other structural locations, due to the thrust-related uplift of such sediments (e.g., porosity of 0.25 at 1.96 km depth BML in well 2 compared to a porosity of 0.31 for the same depth in well 3).

The stress paths in Figure 16 show the stress history of the three points noted in Figure 15. Points x_1 and x_3 are located in laterally compressional regimes with the maximum compression occurring in the in-plane horizontal stress (σ_x'). The stress path for both points is similar, showing an initial period of uniaxial burial before the start of the shortening and a subsequent sharp increase in the deviatoric stress with small changes in the effective mean stress due to the high overpressure generation. The final stress state in x_1 is almost in the critical state. In both cases the final stress state in the deviatoric plane is in a space where $\sigma_x' > \sigma_z' > \sigma_y'$, which is consistent with an Anderson reverse faulting regime (Fossen, 2010). In contrast, the final stress state for point x_2 is in a space where $\sigma_y' > \sigma_z' > \sigma_{x'}'$, evidencing lateral extension in the shortening direction. Initially the stress path follows the uniaxial burial regime as for points x_1 and x_3. Subsequently, there is also a period of layer parallel shortening and lateral compression at this location, which causes the deviatoric stress to increase and the stress path to approach the σ_x' direction in the deviatoric plane. With ongoing shortening and thrust-related uplift, the anticline formation initiates and the stress regime changes to laterally extensional, with a decrease
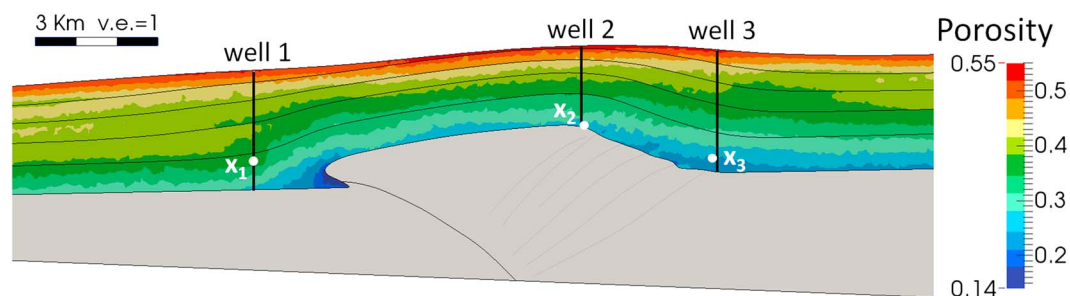

Figure 15. Porosity distribution in the syntectonic sediments at present day with three notional well locations. x_1, x_2, and x_3 indicate the location of three tracked material points.
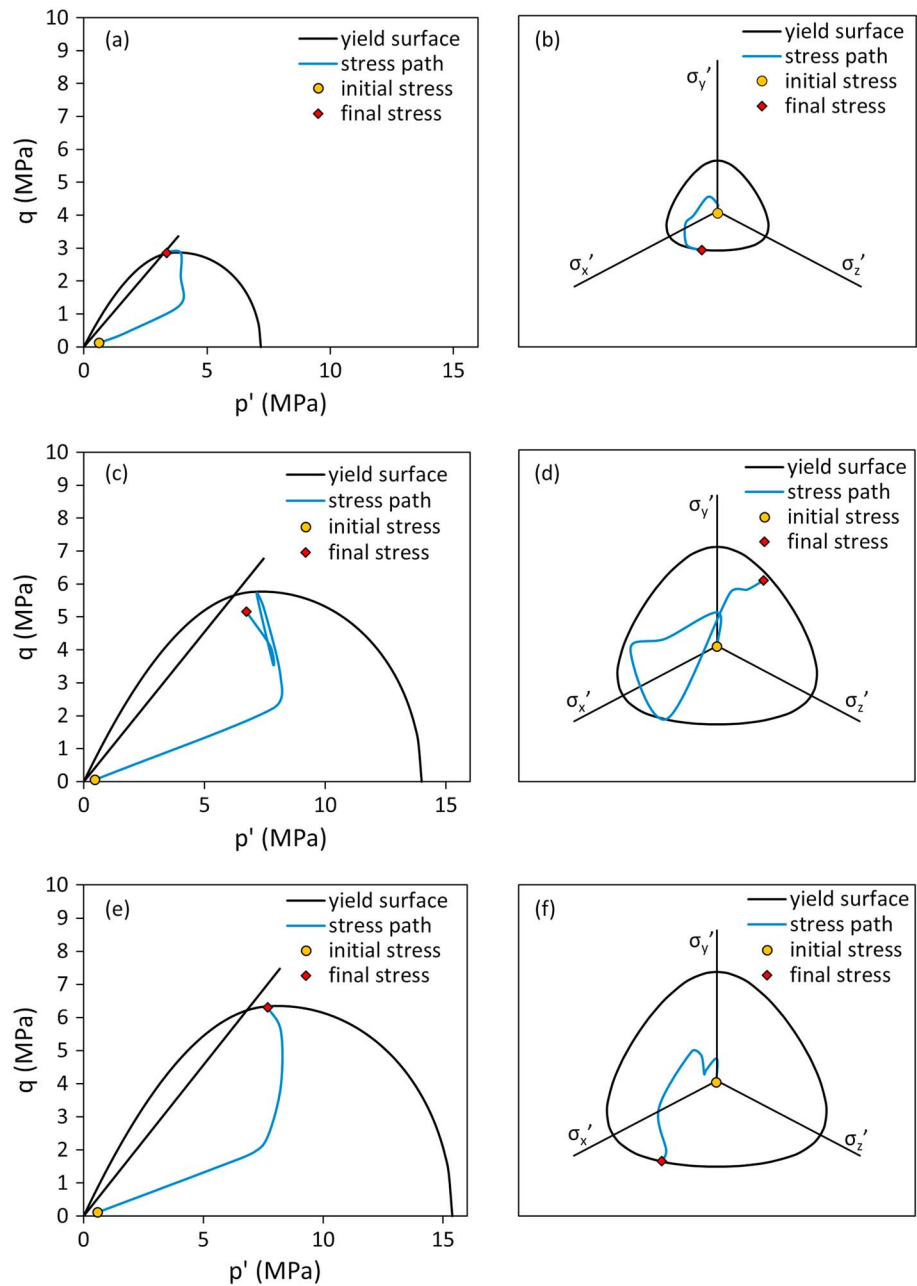
Figure 16. Stress paths for points (a and b) x_1, (c and d) x_2, and (e and f) x_3 from Figure 15. Figures 16a, 16c, and 16e show the stress path in the p'-q plane, whereas Figures 16b, 16d, and 16f show the stress path on the deviatoric plane. The yield surfaces show the final strength of the sediments at present day. Note the similarity in stress paths for the points located in the laterally compressional locations (x_1 and x_3). They show an initial period of uniaxial burial followed by a sharp increase in q with small changes in p' due to the increase in horizontal stress and the high pore pressure generation. Both points approach compressional states in the deviatoric plane ($\sigma_x' > \sigma_z' > \sigma_y'$). In contrast, the stress path for point x_2 approaches a laterally extensional state ($\sigma_y' > \sigma_z' > \sigma_x'$) after an initial period of uniaxial burial followed by layer parallel shortening.

in σ_x' and a decrease in the deviatoric stress. When the magnitude of σ_x' becomes lower than those of σ_y' and σ_z' the deviatoric stress increases until the stress path reaches the final stress state. Such a stress state is typical of a normal faulting regime and reveals a good correlation with the normal faults observed at the crest of some anticlines in the NW Borneo thrust belt.

In Figure 17 the stresses, overpressure, and porosity for the three well locations shown in Figure 15 are compared to facilitate the understanding of the results in terms of the structural location of the well. Well 1 shows
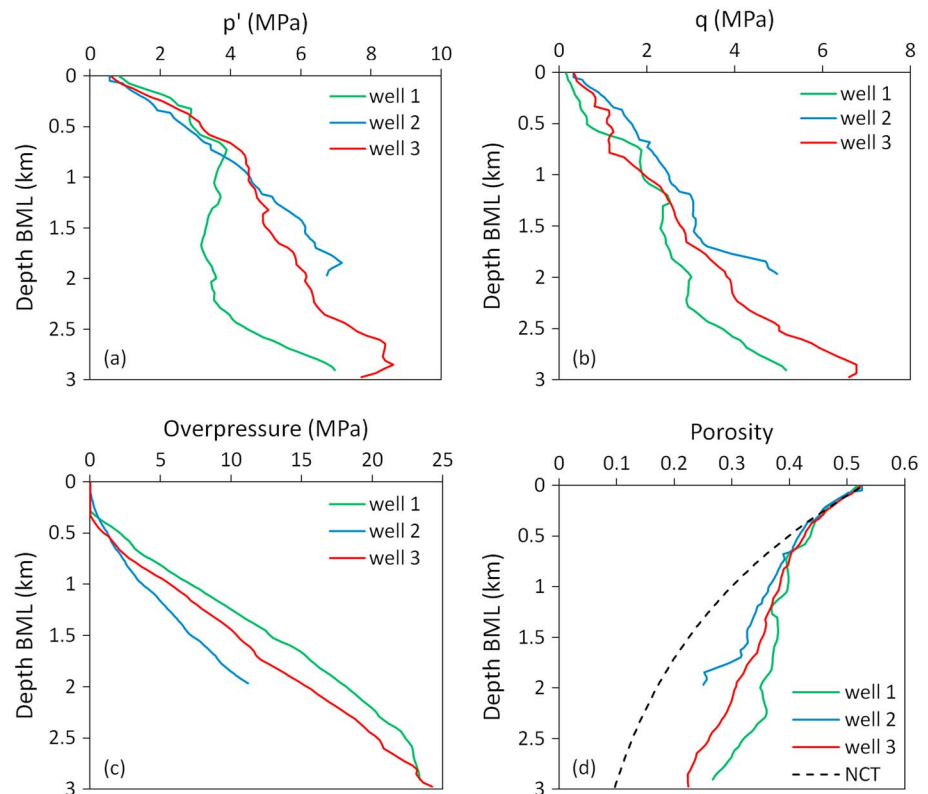
Figure 17. Comparison of the (a) effective mean stress, (b) deviatoric stress, (c) overpressure, and (d) porosity at the three well locations shown in Figure 15. NCT = normal compaction trend.

the lowest effective mean stress at a given depth due to high overpressure developed partly as result of tectonic stress. In addition, this well also shows the lowest deviatoric stress with depth. It is therefore not surprising that the highest porosities are found in well 1. Conversely, well 2 shows the lowest overpressure and the highest effective mean stress and deviatoric stress, which resulted in the lowest porosities out of the three wells. Well 3 shows intermediate values for all the variables. Nonetheless, the overpressure for wells 1 and 3 is equal at a depth of ca. 2.7 km, while the effective mean stress and the deviatoric stress are higher for well 3, with a concomitantly lower porosity. This is likely to be due to the proximity of the deepest sections of well 3 to the youngest kink band. This means that higher lateral stress is found in well 3 at that depth, which is reflected in the higher effective stress ratio values which in turn results in a higher deviatoric stress.

4.5. Overpressure and Porosity Predictions Using Uniaxial Strain Models

In order to assess the predictions using one-dimensional compaction models, we have defined uniaxial strain models for each of the three wells shown in Figure 15. Porosity trends with depth were first obtained at each well location from the thrust model. Then, a decompaction law was applied in order to calculate the layer thickness at deposition. Finally, the duration of the deposition for each layer in the one-dimensional compaction models was kept the same as the layer deposition duration in the thrust model. In this way we preserved the solid sedimentation rate between the uniaxial strain models and the thrust model at each well location.

Notable differences are observed between the overpressure and porosity predictions from the thrust model and the uniaxial strain model at the three well locations (Figure 18). Porosities in all the three well locations are lower than those predicted by their respective one-dimensional compaction models. The maximum porosity difference is 3.5% at a depth of 1.2 km in well 1, 6% at a depth of 1.85 km in well 2, and 7.5% at a depth of 2.5 km in well 3. Overpressure in well 1 is higher than that predicted by the one-dimensional model, with a difference of up to 6.2 MPa at a depth of 2.9 km. In well 2, which is located in the extensional region, overpressure in the top 1.53 km is slightly lower than the 1-D prediction, whereas in deeper sections the overpressure predicted by the thrust model is up to 2.2 MPa higher. Overpressure in the top 0.95 km of well 3 is lower than its corresponding uniaxial strain prediction but is higher with increasing depth and reaches a difference of 6.4 MPa at 2.98 km depth.
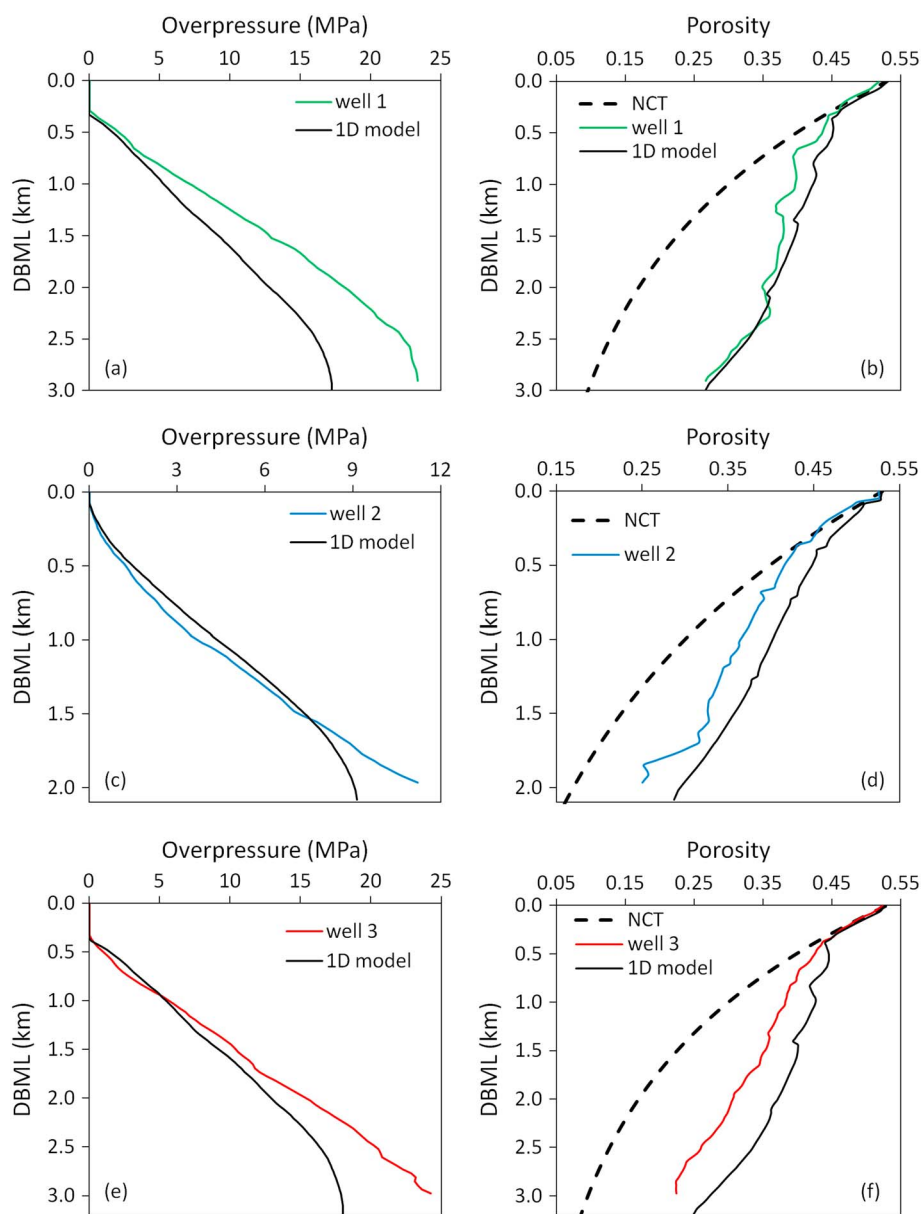
Figure 18. Overpressure and porosity for the three wells shown in Figure 15 compared to the solution obtained from their respective one-dimensional compaction models. (a and b) Well 1, (c and d) Well 2, and (e and f) Well 3.

In general, the thrust model predicted lower porosities and higher overpressures than the uniaxial strain models at laterally compressional locations. The shortening in the thrust model leads to an increase in the total horizontal stress, which in turn leads to an increase in horizontal effective stress, overpressure, or both, depending on the drainage. This contribution of lateral stress in compaction and overpressure generation is not properly accounted for in one-dimensional models, leading to differences in model pore pressure predictions. It is worth mentioning that pore pressure prediction in shales is often addressed by applying one-dimensional methods known as Equivalent Depth Methods (EDM) (Foster, 1966; Hottmann & Johnson, 1965; Yang & Aplin, 2004; Zhang, 2011, 2013). These methods use shale porosity or some porosity-dependent property to compare against a NCT in order to estimate the vertical effective stress and then calculate the overpressure (assuming that the total vertical stress is known and equal to the overburden stress). According to our results, it is anticipated that these methods will not provide accurate predictions in shortening environments. In order to prove that, we have applied the EDM using the porosity trends predicted by the
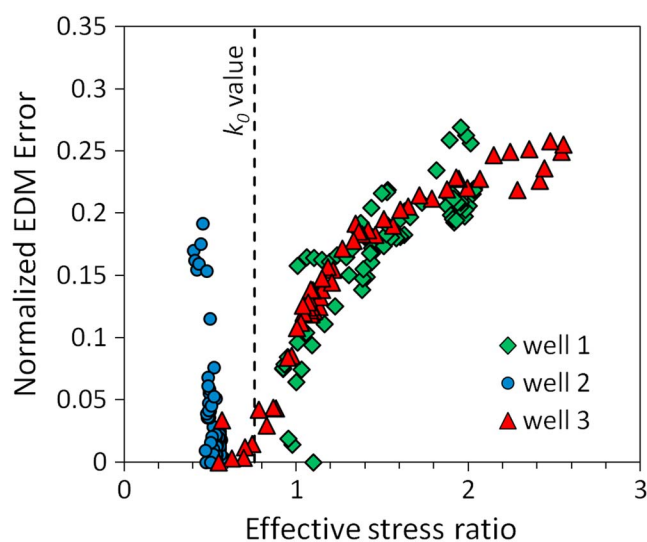
Figure 19. Normalized error in overpressure prediction by the Equivalent Depth Method as a function of the effective stress ratio. The K_0 line shows the value of the effective stress ratio in uniaxial burial conditions.

thrust model at the three well locations shown in Figure 15, obtaining alternative overpressure predictions using 1-D methods. The difference between the thrust model and EDM overpressure predictions is then considered to be the error in EDM prediction due to the assumption of one-dimensional compaction. In Figure 19 we normalized the resulting EDM error against the maximum possible vertical effective stress at each depth (calculated as the lithostatic stress minus the hydrostatic pressures) and plotted it as a function of the effective stress ratio. It is clear that for the laterally compressional wells 1 and 3, the normalized EDM error is positively correlated with effective stress ratio, showing a normalized EDM error increase up to 0.27 as the effective stress ratio increases, thus evidencing the contribution of tectonic stress on overpressure generation and porosity reduction. On the other hand, well 2 shows an almost constant effective stress ratio (which is below the K_0 value) with a normalized EDM error that reaches 0.20. This is because, as mentioned previously, the deep sections of well 2 show relatively low porosities and high overpressures compared to 1-D models. Those were achieved during the early stages of thrust formation. During that period the location was laterally compressional. Then, with the ongoing shortening, the sediments were uplifted and the regime changed to laterally extensional due to the formation of the anticline. Therefore, despite the current stress state reflecting an extensional regime, both the porosity and magnitude of overpressure reflect the earlier compressional regime, explaining the substantial error in pore pressure estimated using the EDM.

5. Conclusions

We have presented coupled geomechanical and fluid flow simulations of a fold-and-thrust structure from NW Borneo. For the first time, we have accounted for both syntectonic sediment deposition and pore pressure evolution due to tectonic deformation in a fold-and-thrust belt. The sediment rheology was modeled with a critical state-based constitutive model that allows the simulation of strain hardening and strain softening with fault localization.

The predicted present-day geometry by the numerical model was consistent with first-order structural features observed in the field. However, some discrepancies were observed: for example, the principal thrust fault did not propagate within the syntectonic sediments, which the model predicts will deform in a ductile manner. These differences are attributed to the omission of nonmechanical hardening effects within the model.

Predicted stresses in syntectonic sediments show two laterally compressive regions located in the thrust front and in the back limb and one laterally extensional region in between, near the axial plane of the anticline that has been formed above the thrust hanging wall. The overpressure contours show the highest values near the two compressional zones. Comparison with uniaxial strain models shows the importance of tectonic compaction, which substantially increased overpressure and decreased porosity at the compressional locations. One-dimensional pore pressure prediction methods are inadequate in tectonic compressive settings.

Pore pressure evolution has been shown to play an important role in structural development. Compared to the coupled model, drained simulations, in which pore pressures are kept hydrostatic through time, predict deformation which is much more ductile in nature, with no thrust fault expression. This is a consequence of the different evolution in the stress paths during tectonic shortening. Due to the high overpressure, in the coupled analysis there is a large increase in the deviatoric stress (the magnitude of which does not depend on overpressure) with small changes in the effective mean stress (the magnitude of which does depend on overpressure), which causes the stress path to meet the yield surface on the shear side, promoting strain localization (faulting). In the drained analysis, there is a greater development of effective mean stress due to the lack of overpressure, which results in the stress path meeting the yield surface on the cap side, thus promoting distributed strain. The sediment consolidation state prior to the onset of overpressure is a key parameter controlling the nature of deformation.

In summary, our results highlight the need to address pore pressure prediction in fold-and-thrust belts using methods capable of accounting for the full stress tensor (Goulty, 2004; Hauser et al., 2014; Obradors-Prats et al., 2017). In addition, comparison of the results obtained from the coupled model with a hydrostatic case reveals the role of overpressure in increasing sediment brittleness, so that pore pressure evolution changes field-scale deformation style. Coupled geomechanical-fluid flow models are thus not only a potentially powerful tool for pore pressure prediction in tectonically active areas but also for understanding controls on the development of major geological structures. Further work is required to expand the available material characterizations in order to incorporate additional first-order factors that control the evolution of overpressure, porosity, and sediment strength.

References

Albertz, M., & Lingrey, S. (2012). Critical state finite element models of contractional fault-related folding: Part 1. Structural analysis. *Tectonophysics*, *576–577*, 133–149.

Albertz, M., & Sanz, P. F. (2012). Critical state finite element models of contractional fault-related folding: Part 2. Mechanical analysis. *Tectonophysics*, *576–577*, 150–170.

Allwardt, J. R., Michael, G. E., Shearer, C. R., Heppard, P. D., & Ge, H. (2009). 2D modeling of overpressure in a salt withdrawal basin, Gulf of Mexico, USA. *Marine and Petroleum Geology*, *26*(4), 464–473.

Aydin, M. G., & Engelder, T. (2014). Revisiting the Hubbert-Rubey pore pressure model for overthrust faulting: Inferences from bedding-parallel detachment surfaces within Middle Devonian gas shale, the Appalachian Basin, USA. *Journal of Structural Geology*, *69*(12), 519–537.

Beaudoin, N., Lacombe, O., Bellahsen, N., Amrouch, K., & Daniel, J. M. (2014). Evolution of pore-fluid pressure during folding and basin contraction in overpressured reservoirs: Insights from the MadisonePhosphoria carbonate formations in the Bighorn Basin (Wyoming, USA). *Marine and Petroleum Geology*, *55*(8), 214–229.

Bilotti, F., & Shaw, J. H. (2005). Deep-water Niger Delta fold and thrust belt modeled as a critical-taper wedge: The influence of elevated basal fluid pressure on structural styles. *AAPG Bulletin*, *89*(11), 1475–1491.

Bolton, A. J., Maltman, A. J., & Clennell, M. B. (1998). The importance of overpressure timing and permeability evolution in fine grained sediments undergoing shear. *Journal of Structural Geology*, *20*(8), 1013–1022.

Bose, S., Mandal, N., Saha, P., Sarkar, S., & Lithgow-Bertelloni, C. (2014). Thrust initiation and its control on tectonic wedge geometry: An insight from physical and numerical models. *Journal of Structural Geology*, *67*(10), 37–49.

Cardozo, N., & Brandenburg, J. P. (2014). Kinematic modeling of folding above listric propagating thrusts. *Journal of Structural Geology*, *60*(3), 1–12.

Cobbold, P. R., & Castro, L. (1999). Fluid pressure and effective stress in sandbox models. *Tectonophysics*, *301*(1–2), 1–19.

Cobbold, P. R., Clarke, B. J., & Loseth, H. (2009). Structural consequences of fluid overpressure and seepage forces in the outer thrust belt of the Niger Delta. *Petroleum Geoscience*, *15*(1), 3–15.

Cobbold, P. R., Durand, S., & Mourgues, R. (2001). Sandbox ming of thrust wedges with fluid-assisted detachments. *Tectonophysics*, *334*(3–4), 245–258.

Cobbold, P. R., Mourgues, R., & Boyd, K. (2004). Mechanism of thin-skinned detachment in the Amazon Fan: Assessing the importance of fluid overpressure and hydrocarbon generation. *Marine and Petroleum Geology*, *21*(8), 1013–1025.

Corredor, F., Shaw, J. H., & Bilotti, F. (2005). Structural styles in the deep-water fold and thrust belts of the Niger Delta. *AAPG Bulletin*, *89*(6), 753–780.

Cotecchia, F., & Chandler, R. J. (1997). The influence of structure on the pre-failure behaviour of a natural clay. *Géotechnique*, *47*(3), 523–544.

Couzens-Schultz, B. A. K., & Azbel, K. (2014). Predicting pore pressure in active fold-thrust systems: An empirical model for the deepwater Sabah fold belt. *Journal of Structural Geology*, *69*, 465–480.

Crook, A. J. L. (2013). *ParaGeo: A finite element model for coupled simulation of the evolution of geological structures*. Swansea, UK: Three Cliffs Geomechanical Analysis.

Daniel, R. B. (2001). Pressure prediction for a Central Graben wildcat well, UK North Sea. *Marine and Petroleum Geology*, *18*(2), 235–250.

Einstein, H. H., & Dershowitz, W. S. (1990). Tensile and shear fracturing in predominantly compressive stress fields — A review. *Engineering Geology*, *29*, 149–172.

Flemings, P. B., & Lupa, J. A. (2004). Pressure prediction in the Bullwinkle Basin through petrophysics and flow modeling (Green Canyon 65, Gulf of Mexico). *Marine and Petroleum Geology*, *21*(10), 1311–1322.

Fossen, H. (2010). *Chapter 5: Stress in the lithosphere. Structural geology* (Vol. 463). Cambridge: Cambridge University Press.

Foster, J. B. (1966). Estimation of formation pressures from electrical surveys-offshore Louisiana. *Marine and Petroleum Geology*, *18*(2), 165–171.

Franke, D., Barckhausen, U., Heyde, I., Tingay, M., & Ramli, N. (2008). Seismic images of a collision zone offshore NW Sabah/Borneo. *Marine and Petroleum Geology*, *25*, 606–624.

Goulty, N. R. (2004). Mechanical compaction behaviour of natural clays and implications for pore pressure estimation. *Petroleum Geoscience*, *10*(1), 73–79.

Hall, R., & Morley, C. K. (2004). Sundaland basins. In Clift, P., Wang, P., Kuhnt, W., & Hayes, D. (Eds.), *Continent-ocean interactions within East Asian marginal seas, Geophusical Monograph Series* (Vol. 149, pp. 55–85). Washington, DC: American Geophysical Union.

Hauser, M. R., Couzens-Schultz, B. A., & Chan, A. W. (2014). Estimating the influence of stress state on compaction behavior. *Geophysics*, *79*(6), 389–398.

Hennig, A., Yassir, N. A., Addis, M. A., & Warrington, A. (2002). Pore-pressure estimation in an active thrust region and its impact on exploration and drilling. In Huffman, A. R. & Bowers, G. L. (Eds.), *Pressure regimes in sedimentary basins and their prediction, AAPG memoir* (Vol. 76, pp. 89–105). AAPG.

Hesse, S., Back, S., & Franke, D. (2009). The deep-water fold-and-thrust belt offshore NW Borneo: Gravity-driven versus basement-driven shortening. *Geological Society of America Bulletin*, *121*(5/6), 939–953.

Hesse, S., Back, S., & Franke, D. (2010). The structural evolution of folds in a deepwater fold and thrust belt — A case study from the Sabah continental margin offshore NW Borneo, SE Asia. *Marie and Petroleum Geology*, *27*(2), 442–454.

Hottmann, C. E., & Johnson, R. K. (1965). Estimation of formation pressures from log-derived shale properties. *Journal of Petroleum Technology*, *17*(06), 717–722.

Hubbert, M. K., & Rubey, W. W. (1959). Role of fluid pressure in mechanics of overthrust faulting. *Geological Society of America Bulletin*, *70*, 115–166.

Ingram, G. M., Chisholm, T. J., Grant, C. J., Hedlund, C. A., Stuart-Smith, P., & Teasdale, J. (2004). Deepwater north west Borneo: Hydrocarbon accumulation in an active fold and thrust belt. *Marine and Petroleum Geology*, *21*(7), 879–887.

Ishii, E., Sanada, H., Iwatsuki, T., Sugita, Y., & Kurikami, H. (2011). Mechanical strength of the transition zone at the boundary between opal-A and opal-CT zones in siliceous rocks. *Engineering Geology*, *122*, 214–221.

King, R. C., Hillis, R. R., Tingay, M. R. P., & Morley, C. K. (2009). Present-day stress and neotectonic provinces of the Baram delta and deep-water fold-thrust belt. *Journal of the Geological Society (London, U.K.)*, *166*, 197–200.

Krueger, S., & Grant, N. (2011). The growth history of toe thrusts of the Niger Delta and the role of pore pressure. In McClay, K., Shaw, J., & Suppe, J. (Eds.), *Thrust fault-related folding, AAPG memoir* (Vol. 94, pp. 357–390). AAPG.

Maloney, D., Davies, R., Imber, J., Higgins, S., & King, S. (2010). New insights into deformation mechanisms in the gravitationally driven Niger Delta deep-water fold and thrust belt. *AAPG Bulletin*, *94*(9), 1401–1424.

McClay, K. R., Whitehouse, P. S., Dooley, T., & Richards, M. (2004). 3D evolution of fold and thrust belts formed by oblique convergence. *Marine and Petroleum Geology*, *21*(7), 857–877.

Mitra, S. (1990). Fault-propagation folds: Geometry, kinematic evolution, and hydrocarbon traps. *AAPG Bulletin*, *74*(6), 921–945.

Morley, C. (2009). Geometry of an oblique thrust fault zone in a deepwater fold belt from 3D seismic data. *Journal of Structural Geology*, *31*(12), 1540–1555.

Morley, C. K., Tingay, M., Hillis, R., & King, R. (2008). Relationship between structural style, overpressures, and modern stress, Baram Delta Province, northwest Borneo. *Journal of Geophysical Research*, *113*, B09410. https://doi.org/10.1029/2007JB005324

Mourgues, R., & Cobbold, P. R. (2006). Thrust wedges and fluid overpressures: Sandbox models involving pore fluids. *Journal of Geophysical Research*, *111*, B05404. https://doi.org/10.1029/2004JB003441

Neumaier, M., Littke, R., Hantschel, T., Maerten, L., Joonnekindt, J., & Kukla, P. (2014). Integrated charge and seal assessment in the Monagas fold and thrust belt of Venezuela. *AAPG Bulletin*, *98*(7), 1325–1350.

Nikolinakou, M. A., Flemings, P. B., & Hudec, M. R. (2014). Modeling stress evolution around a rising salt diapir. *Marine and Petroleum Geology*, *51*, 230–238.

Nygård, R., Gutierrez, M., Bratli, R. K., & Høeg, K. (2006). Brittle-ductile transition, shear failure and leakage in shales and mudrocks. *Marine and Petroleum Geology*, *23*(2), 201–212.

Obradors-Prats, J., Rouainia, M., Aplin, A. C., & Crook, A. J. L. (2016). Stress and pore pressure histories in complex tectonic settings predicted with coupled geomechanical-fluid flow models. *Marine and Petroleum Geology*, *76*, 464–477.

Obradors-Prats, J., Rouainia, M., Aplin, A. C., & Crook, A. J. L. (2017). Assessing the implications of tectonic compaction on pore pressure using a coupled geomechanical approach. *Marine and Petroleum Geology*, *79*, 31–43.

Roberts, D. T., Crook, A. J. L., Profit, M. L., & Cartwright, J. A. (2015). Investigating the evolution of polygonal fault systems using geomechanical forward modeling. In *49th US Rock Mechanics/Geomechanics Symposium*, San Francisco, CA.

Roscoe, K. H., & Burland, J. B. (1968). On the generalised stress-strain behaviour of wet clay. In Heyman, J. J. & Leckie, F. A. (Eds.), *Engineering plasticity* (pp. 535–609). Cambridge, UK: Cambridge University Press.

Shaw, J. H., Bilotti, F., & Brennan, P. A. (1999). Patterns of imbricate thrusting. *Geological Society of America Bulletin*, *111*(8), 1140–1154.

Sibson, R. H. (2003). Brittle-failure controls on maximum sustainable overpressure in different tectonic regimes. *AAPG Bulletin*, *87*(6), 901–908.

Simmons, W. J. F., Socquet, A., Vigny, C., Ambrosius, B. A. C., Haji Abu, S., Promthong, C., . . . Spakman, W. (2007). A decade of GPS in Southeast Asia: Resolving Sundaland motion and boundaries. *Journal of Geophysical Research*, *112*, B06420. https://doi.org/10.1029/2005JB003868

Smart, K. J., Ferrill, D. A., Morris, A. P., & McGinnis, R. N. (2012). Geomechanical modeling of stress and strain evolution during contractional fault-related folding. *Tectonophysics*, *576-577*, 171–196.

Suppe, J., & Medwededd, D. A. (1990). Geometry and kinematics of fault-propagation folding. *Eclogae Geologicae Helvetiae*, *83*(3), 409–454.

Terzaghi, K. (1923). Die Berechnung der Durchlässigkeitsziffer des Tones aus dem Verlauf der hydrodynamischen Spannungserscheinungen. *Sitzungsberichte Akademie der Wissenschaften in Wien*, *132*, 125–138.

Thornton, D. A., & Crook, A. J. L. (2014). Predictive modelling of the evolution of fault structure: 3-D modelling and coupled geomechanical/flow simulation. *Rock Mechanics and Rock Engineering*, *47*(5), 1533–1549.

Tingay, M. R. P., Hillis, R. R., Morley, C. K., Swarbrick, R. E., & Drake, S. J. (2005). Present day stress orientations in Brunei: A snapshot of prograding tectonics in a Tertiary delta. *Journal of the Geological Society (London, U.K.)*, *162*, 39–49.

van Ruth, P. J., Hillis, R. R., & Swarbrick, R. E. (2002). Detecting overpressure using porosity-based techniques in the Carnarvon basin, Australia. In *APPEA Conference, Australian Petroleum Production and Exploration Association* (pp. 559–569). Adelaide, Australia.

Ventouras, K., & Coop, M. R. (2009). On the behaviour of Thanet Sand: An example of an uncemented natural sand. *Géotechnique*, *59*, 727–738.

Wood, D. M. (1990). *Soil behaviour and critical state soil mechanics*. Cambridge: Cambridge University Press.

Yang, Y., & Aplin, A. C. (2004). Definition and practical application of mudstone porosity-effective stress relationships. *Petroleum Geoscience*, *10*, 153–162.

Yang, Y., & Aplin, A. C. (2010). A permeability-porosity relationship for mudstones. *Marine and Petroleum Geology*, *27*(8), 1692–1697.

Zanella, A., Cobbold, P. R., & Le Carlier de Veslud, C. (2014). Physical modelling of chemical compaction, overpressure development, hydraulic fracturing and thrust detachments in organic rich source rock. *Marine and Petroleum Geology*, *55*(8), 262–274.

Zhang, J. (2011). Pore pressure prediction from well logs: Methods, modifications, and new approaches. *Earth-Science Reviews*, *108*(1–2), 50–63.

Zhang, J. (2013). Effective stress, porosity, velocity and abnormal pore pressure prediction accounting for compaction disequilibrium and unloading. *Marine and Petroleum Geology*, *45*(8), 2–11.